



Physical: Letter

# Direct imaging of lithium atoms in LiV<sub>2</sub>O<sub>4</sub> by spherical aberration-corrected electron microscopy

Yoshifumi Oshima<sup>1,2,\*</sup>, Hidetaka Sawada<sup>1,3</sup>, Fumio Hosokawa<sup>1,3</sup>, Eiji Okunishi<sup>1,3</sup>, Toshikatsu Kaneyama<sup>1,3</sup>, Yukihito Kondo<sup>1,3</sup>, Seiji Niitaka<sup>4</sup>, Hidenori Takagi<sup>4</sup>, Yasumasa Tanishiro<sup>1,5</sup> and Kunio Takayanagi<sup>1,5</sup>

<sup>1</sup>Japan Science and Technology Agency, CREST, 5 Sanbancho, Chiyoda-ku, Tokyo, 102-0075, Japan,

<sup>2</sup>Department of Materials Science and Engineering, Tokyo Institute of Technology, 4259-J1-3 Nagatsuta, Midori-ku, Yokohama 226-8502, Japan, <sup>3</sup>JEOL Ltd, 3-1-2 Musashino, Akishima, Tokyo, 196-8558, Japan,

<sup>4</sup>Magnetic Materials Laboratory, RIKEN, 2-1 Hirosawa, Wako, Saitama 351-0198, Japan <sup>5</sup>Department of Condensed Matter Physics, Tokyo Institute of Technology, 2-12-1-H-51 Oh-okayama, Meguro-ku, Tokyo 152-8551, Japan

\*To whom correspondence should be addressed. E-mail: oshima.y.aa@m.titech.ac.jp

**Abstract**

We visualized lithium atom columns in LiV<sub>2</sub>O<sub>4</sub> crystals by combining scanning transmission electron microscopy with annular bright field (ABF) imaging using a spherical aberration-corrected electron microscope (R005) viewed from the [110] direction. The incident electron beam was coherent with a convergent angle of 30 mrad (semi-angle), and the detector collected scattered electrons over 20–30 mrad (semi-angle). The ABF image showed dark dots corresponding to lithium, vanadium and oxygen columns.

**Keywords**

aberration correction, cold field emission gun, scanning transmission electron microscopy, lithium, spinel structure, annular bright field microscopy

**Received**

14 January 2010, accepted 30 March 2010, online 20 April 2010

Rechargeable lithium-ion batteries are key components of portable electronic devices. Because LiM<sub>2</sub>O<sub>4</sub> (M: transition metal ion), which has a spinel structure, provides a three-dimensional tunnel for lithium diffusion [1,2], its potential as a cathodic material for batteries has been noted, but implementation of such a material has been delayed due to its limited cycling and unsatisfactory storage performance at elevated temperatures [3] as lithium ions are inserted into or extracted from host materials during battery operation. Thus, to improve battery performance, it is important to visualize the behaviour of lithium atoms in and around host materials. Recently, electron energy-loss spectroscopy has been used to clarify the dynamic behaviour of lithium distribution on the nanometre scale during the charge–discharge cycle in Li<sub>1.2</sub>Mn<sub>0.4</sub>Fe<sub>0.4</sub>O<sub>2</sub> [4]. Unfortunately, the resolution of the experiment did not reach the atomic level.

High spatial resolution on the order of several tens of picometres has been applied to image materials containing lithium atoms at the atomic level by retrieving the exiting wave phase of a specimen from a focal series of high-resolution transmission electron microscope (TEM) images [5]. This method has been used to resolve lithium atomic columns in LiCoO<sub>2</sub> crystals [6]. Using an aberration-corrected TEM, lithium atomic columns in Al<sub>3</sub>Li precipitates have been clearly visualized [7]. On the other hand, high-angle annular dark field (HAADF) images have been unsuccessful in imaging lithium atomic columns even with a spherical aberration-corrected electron microscope. Because the intensity at each atomic column strongly correlates with the atomic number ( $Z$ ) [8,9], light ele-

ments are less intense than heavy elements. In HAADF, lithium column sites in LiFePO<sub>4</sub> have been visualized by exchanging 15% of the Li atoms with Fe atoms [10]. Recently, aberration-corrected scanning transmission electron microscopy (STEM) imaging using an annular detector located within the bright field region has been reported to visualize oxygen columns, strontium columns and titanium oxide columns in a SrTiO<sub>3</sub> crystal [11]. This annular bright field (ABF) imaging, which takes advantage of the large convergent angle of the incident beam, is an interesting approach to imaging lithium atomic columns located near columns of heavy elements.

In this study, we visualized lithium atom columns in LiV<sub>2</sub>O<sub>4</sub> crystals (space group of  $F_{d\bar{3}m}$  and lattice constant of 0.824 nm) by ABF imaging with our spherical aberration-corrected electron microscope (R005) [12] that enabled a dumbbell shape in the HAADF image, which corresponds to a pair of germanium atomic columns aligned to the [114] direction with a 47-pm spacing, to be resolved [13]. We observed the lithium, vanadium and oxygen columns by viewing the LiV<sub>2</sub>O<sub>4</sub> crystals from the [110] direction.

As shown in Fig. 1, vanadium columns are located at both V <sub>$\alpha$</sub>  sites (denoted by the purple spheres) and V <sub>$\beta$</sub>  sites (denoted by the light purple spheres). The blue lines show a rhombic unit which connects V <sub>$\alpha$</sub>  sites at the corner. Each V <sub>$\alpha$</sub>  column contains two vanadium atoms per unit cell length along the [110] direction (0.58 nm), whereas each V <sub>$\beta$</sub>  column contains one atom. Along the horizontal diagonal line of the rhombic unit (parallel to the [001] direction), two lithium columns (green spheres) are located between two oxygen columns (red spheres) with a distance between adjacent columns of 0.103 nm. Along the [110] direction, there are one lithium atom and two oxygen atoms per unit length (0.58 nm).

To prevent electron irradiation damage to the specimen, the STEM probe had a relatively low current of 10 pA. The probe was converged with a semi-angle of 30 mrad, within the range of which the electron beam is determined to be coherent by the Ronchigram. ABF images were obtained by collecting electrons scattered between 20 and 30 mrad in the semi-angle. The detection angle was limited by a handmade aperture. The HAADF images, which had a detection angle ranging from 75 to 200 mrad,

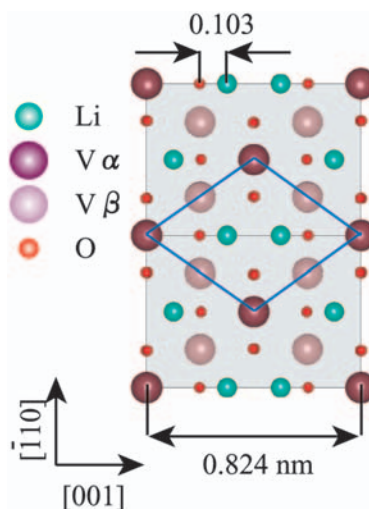


**Fig. 1.** Schematic illustration of LiV<sub>2</sub>O<sub>4</sub> crystal atomic structure as viewed from the [110] direction. The shaded area is the projection of the unit cell. Purple and light purple spheres indicate vanadium columns at V <sub>$\alpha$</sub>  sites (at the corner of the rhombic unit illustrated by blue lines) and V <sub>$\beta$</sub>  site, respectively. Small red spheres indicate oxygen columns. Green spheres are lithium columns. Along the diagonal line of each rhombic unit ([001] direction), a vanadium, an oxygen, two lithium, an oxygen and a vanadium columns are aligned. The lithium column is 0.103 nm from the oxygen column, and the oxygen column is 0.206 nm from the V <sub>$\alpha$</sub>  column. Each column has atoms of the same element. The vanadium (V <sub>$\alpha$</sub> ) and oxygen columns contain two atoms within the unit length (0.58 nm), and the vanadium (V <sub>$\beta$</sub> ) and lithium columns contain one atom.

were simultaneously obtained with the ABF images. The dwell time per pixel was 38  $\mu$ s. The size of each pixel was 16.5 pm. Single LiV<sub>2</sub>O<sub>4</sub> crystals were grown via the flux method [14]. The LiV<sub>2</sub>O<sub>4</sub> crystals were crushed in ethanol, and the specimens were prepared by desiccating a drop of this suspension onto a holey carbon support film.

In Fig. 2a and b are simultaneously acquired raw ABF and HAADF images from the same region viewed from the [110] direction, respectively. The specimen is wedge shaped, and the observed region is in the vicinity of the edge. The atomic columns appear as dark dots in the ABF image (Fig. 2a), although they are bright dots in the HAADF image (Fig. 2b). In Fig. 2b, the intensity of the bright dots increases monotonously along the [110] direction from the top to the bottom of the panel in relation to the increase in thickness along the [110] direction. These bright dots, which form the network of rhombic units shown in Fig. 1, are assigned as vanadium V <sub>$\alpha$</sub>  sites. The white lines denote a rhombic unit. In the ABF image, the vanadium columns at the V <sub>$\alpha$</sub>  sites appear as dark dots. In the rhombic unit, two dots,

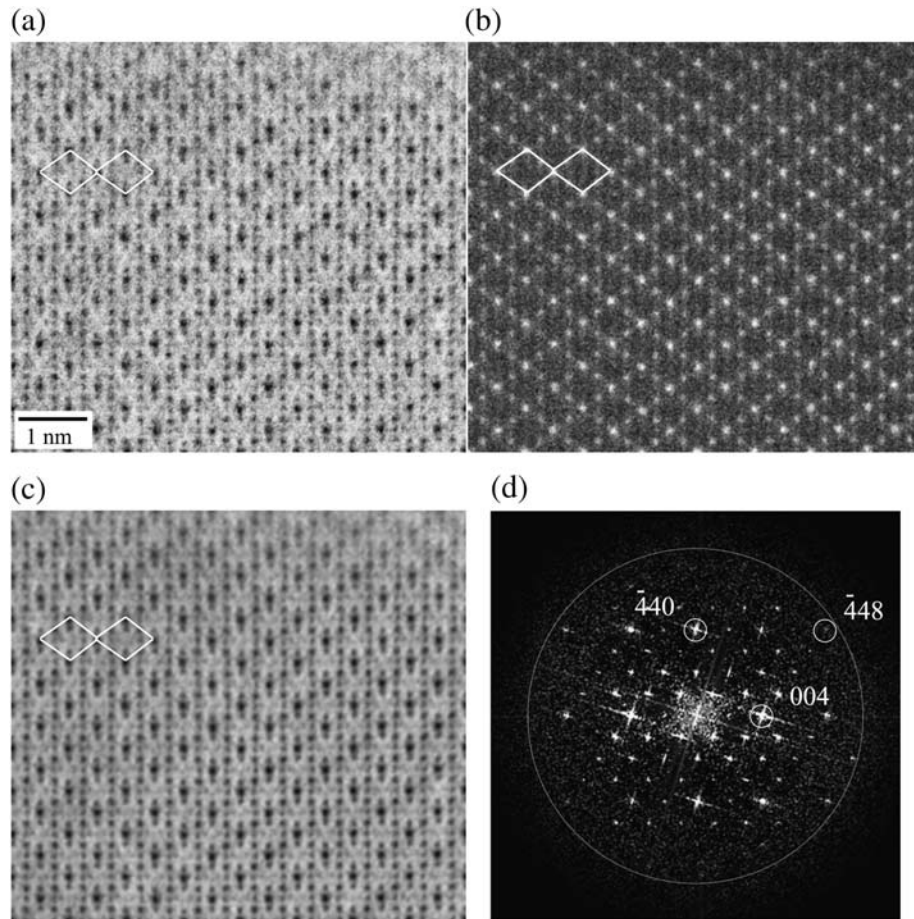


**Fig. 2.** (a) and (b) Raw ABF and HAADF images of  $\text{LiV}_2\text{O}_4$  crystal viewed from the [110] direction. The area is  $6.59 \times 5.43 \text{ nm}^2$ . White lines indicate the rhombic unit illustrated in Fig. 1. (c) Processed ABF image. (d) Fourier transform of the processed ABF image. The highest index of the reflection spot is  $\bar{4}48$ , which corresponds to  $(84 \text{ pm})^{-1}$ . The  $004$  spot and  $\bar{4}40$  spot correspond to  $(206 \text{ pm})^{-1}$  and  $(146 \text{ pm})^{-1}$ , respectively. Large circle indicates the frequency filter set at  $(80 \text{ pm})^{-1}$ .

which are along the diagonal line parallel to the [001] direction, are located at the same position as the oxygen columns in Fig. 1. Furthermore, the two weak dots between two oxygen columns are assigned to the lithium columns.

Figure 2c is the processed ABF image of Fig. 2a, which was obtained after employing a radial difference filter and a frequency filter to the raw image. The radial difference filter subtracts the noisy background using the method described in references [15,16], while the frequency filter passes reciprocal wavelengths below  $(80 \text{ pm})^{-1}$  with the edge smoothed from  $(80 \text{ pm})^{-1}$  to  $(67 \text{ pm})^{-1}$ . Therefore, periodical spots below  $(80 \text{ pm})^{-1}$  are maintained as shown in the Fourier transform of Fig. 2d. The vanadium, oxygen and lithium atomic columns are more clearly observed (Supplementary Fig. 1) in the processed ABF image of Fig. 2c than Fig. 2a due to the lower noise level in Fig. 2c.

Figure 3a is an enlarged raw image. Along the horizontal line ([001] direction), which connects  $\text{V}_{\alpha}$  columns located at the corner of each rhombic unit, two weak dots are seen between two oxygen columns; these dots correspond to the sites of the lithium columns. Figure 3b is the processed image of the same region. The dark dots for the lithium columns are clearly observed. The right panel shows the intensity profile along the [001] direction. In the profile, image contrast of the dark dots is reversed and displayed as peaks. We find that the peaks appear at the vanadium ( $\text{V}_{\alpha}$ ), oxygen and lithium columns. Among 240 lithium columns (the  $8 \times 15$  rhombic units) in the processed image, 220 columns showed peaks discriminating from the peaks of the neighbouring oxygen columns. The intensities for each of the vanadium ( $\text{V}_{\alpha}$ ), oxygen and lithium columns gave the histogram, which showed that the peak ratio of these columns was about 4:2:1 (Supplementary Fig. 2).

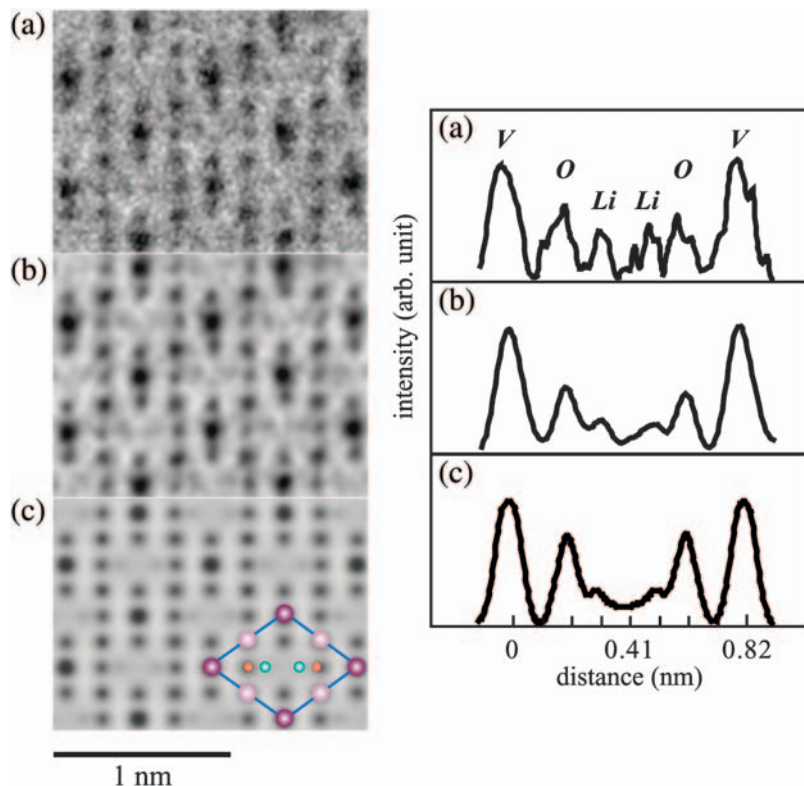


**Fig. 3.** Enlarged ABF image of a  $\text{LiV}_2\text{O}_4$  crystal viewed from the [110] direction. (a) Raw ABF image and (b) Processed ABF image. (c) Simulated ABF image. The right panel shows the intensity profiles along the [001] direction (width of 1 pixel = 16.5 pm). In the profile, image contrast of the dark dots is inverted and displayed as peaks.

In the raw ABF image of Fig. 2a, the intensity profiles along the diagonal lines of 120 rhombic units, after averaging, gave a curve shown in Fig. 3b. The intensity ratio of vanadium ( $\text{V}_{\alpha}$ ), oxygen and lithium columns was also 4:2:1. Thus, the lithium column has been observed with high contrast above the noise level (Supplementary Fig. 2). This suggests that the observed dark dots in the ABF image represent the real existence of the lithium atomic columns.

We simulated an ABF image of a  $\text{LiV}_2\text{O}_4$  crystal using a multi-slice calculation and the following experimental parameters: a convergent semi-angle of the incident electron beam of 30 mrad and a detection angle of 20–30 mrad in the semi-angle. The simulated image was convoluted with a Gaussian function of 16 pm at full width at half maximum [17] because the estimated Gaussian probe size for the cold field emission emitter of the R005 microscope was 16 pm [13]. The uncertain parameters in the experiment were specimen thickness and defocus. We simulated ABF images for thicknesses from 3 to 12 nm in 3-nm steps and defoci amounts from 3 nm (over-focus) to -3 nm (under-focus) in

1-nm steps. The change in the intensity ratio between the vanadium, oxygen and lithium columns is negligible as the thickness varies at a constant focus value. On the other hand, varying the focus at a constant thickness causes the intensity profile of each column to be sharper for a defocus range from the in-focus to 1-nm over-focus. These results are similar to those in a previous report [18]. Additionally, the simulated results agree well with the observed ABF image where the lithium columns in the entire area in Fig. 2 are visible regardless of the specimen thickness.

Quantitatively, the intensity ratio in the simulation is about 4:3:1, as shown in the profile of Fig. 3c. The relative intensities of the lithium to the vanadium column at the  $\text{V}_{\alpha}$  site are the same in the simulation and observation, while the intensity of the oxygen column is higher in the simulation than in the observation. The dark contrast at the lithium column is not an artefact, but shows the existence of the lithium atom. When lithium atoms are assumed to be totally deficit, the simulated ABF image does not exhibit contrast at the lithium sites. Hence, we con-

clude that the two weak dots between the oxygen columns in the ABF image are lithium columns, although the quantitative disagreement between the experiment and theoretical calculation remains to be clarified.

In conclusion, lithium atom columns in  $\text{LiV}_2\text{O}_4$  crystals have been visualized by ABF imaging from the [110] direction of the crystal using a spherical aberration-corrected electron microscope (R005). Vanadium, oxygen and lithium atomic columns appear as dark dots in the ABF image. The intensity ratio of vanadium at the rhombic lattice sites, oxygen and lithium is 4:2:1 in the experiment.

## Funding

This work was supported by the Japan Science and Technology Agency (JST) under the CREST project.

## Supplementary data

Supplementary data is available at <http://jmicro.oxfordjournals.org/>.

## References

- 1 Thackeray M M, de Kock A, Rossouw M H, Liles D, Bittihn R, and Hoge D (1992) Spinel electrodes from the Li-Mn-O system for rechargeable lithium battery applications. *J. Electrochem. Soc.* **139**: 363–366.
- 2 Wang G X, Bradhurst D H, Dou S X, and Liu H K (1999) Spinel  $\text{Li}[\text{Li}_{1/3}\text{Ti}_{5/3}]\text{O}_4$  as an anode material for lithium ion batteries. *J. Power Sources* **83**: 156–161.
- 3 Tarascon J M and Armand M (2001) Issues and challenges facing rechargeable lithium batteries. *Nature* **414**: 359–367.
- 4 Kikkawa J, Akita T, Tabuchi M, Shikano M, Tatsumi K, and Kohyama M (2008) Real-space observation of Li extraction/insertion in  $\text{Li}_{1.2}\text{Mn}_{0.4}\text{Fe}_{0.4}\text{O}_2$  positive electrode material for Li-ion batteries. *Electrochim. Solid-State Lett.* **11**: A183–A186.
- 5 Coene W, Janssen G, Op de Beeck M, and Van Dyck D (1992) Phase retrieval through focus variation for ultra-resolution in field-emission transmission electron microscopy. *Phys. Rev. Lett.* **69**: 3743.
- 6 Shao-Horn Y, Crogueennec L, Delmas C, Nelson E C, and O'Keefe M A (2003) Atomic resolution of lithium ions in  $\text{LiCoO}_2$ . *Nat. Mater.* **2**: 464–467.
- 7 Rossell M D, Erni R, Asta M, Radmilovic V, and Dahmen U (2009) Atomic-resolution imaging of lithium in  $\text{Al}_3\text{Li}$  precipitates. *Phys. Rev. B* **80**: 024110.
- 8 Varela M, Lupini A R, Benthem Kv, Borisevich A Y, Chisholm M F, Shibata N, Abe E, and Pennycook S J (2005) Materials characterization in the aberration-corrected scanning transmission electron microscope. *Annu. Rev. Mater. Res.* **35**: 539–569.
- 9 Mkobyan K A, Batson P E, Cha J, Schaff W J, and Silcox J (2006) Direct determination of local lattice polarity in crystals. *Science* **312**: 1354.
- 10 Chung S-Y, Choi S-Y, Yamamoto T, and Ikuhara Y (2008) Atomic-scale visualization of antisite defects in  $\text{LiFePO}_4$ . *Phys. Rev. Lett.* **100**: 125502–125504.
- 11 Okunishi E, Ishikawa I, Sawada H, Hosokawa F, Hori M, and Kondo Y (2009) Visualization of light elements at ultrahigh resolution by STEM annular bright field microscopy. *Microsc. Microanal.* **15**: 164–165.
- 12 Sawada H, Hosokawa F, Kaneyama T, Ishizawa T, Terao M, Kawazoe M, Sannomiya T, Tomita T, Kondo Y, Tanaka T, Oshima Y, Tanishiro Y, Yamamoto N, and Takayanagi K (2007) Achieving 63 pm resolution in scanning transmission electron microscope with spherical aberration corrector. *Jpn. J. Appl. Phys.* **46**: L568.
- 13 Sawada H, Tanishiro Y, Ohashi N, Tomita T, Hosokawa F, Kaneyama T, Kondo Y, and Takayanagi K (2009) STEM imaging of 47-pm-separated atomic columns by a spherical aberration-corrected electron microscope with a 300-kV cold field emission gun. *J. Electron Microsc. (Tokyo)* **58**: 357–361.
- 14 Matsushita Y, Ueda H, and Ueda Y (2005) Flux crystal growth and thermal stabilities of  $\text{LiV}_2\text{O}_4$ . *Nat. Mater.* **4**: 845–850.
- 15 Kilaas R (1998) Optimal and near-optimal filters in high-resolution electron microscopy. *J. Microsc.* **190**: 45–51.
- 16 Ishizuka K, Eilers P, and Kogure T (2007) Optimal noise filters in high-resolution electron microscopy. *Microsc. Microanal.* **13**: 902–903.
- 17 Nellist P D and Rodenburg J M (1994) Beyond the conventional information limit: the relevant coherence function. *Ultramicroscopy* **54**: 61–74.
- 18 Findlay S D, Shibata N, Sawada H, Okunishi E, Kondo Y, Yamamoto T, and Ikuhara Y (2009) Robust atomic resolution imaging of light elements using scanning transmission electron microscopy. *Appl. Phys. Lett.* **95**: 191913–191913.